


# Identification and analysis of very-large-scale turbulent motions using multiscale proper orthogonal decomposition

Cheng Chi\* and Dominique Thévenin 

*Laboratory of Fluid Dynamics and Technical Flows,  
University of Magdeburg “Otto von Guericke,” D-39106 Magdeburg, Germany*

Alexander J. Smits 

*Department of Mechanical and Aerospace Engineering,  
Princeton University, Princeton, New Jersey 08544, USA*

Steve Wolligandt and Holger Theisel

*Faculty of Computer Science, University of Magdeburg  
“Otto von Guericke,” D-39106 Magdeburg, Germany*



(Received 15 April 2022; accepted 2 August 2022; published 15 August 2022)

To identify and characterize very-large-scale motions (VLSM) in turbulent channel flows, direct numerical simulations are performed at  $Re_\tau = 906$  and 3216. The turbulence structure is then analyzed by proper orthogonal decomposition (POD) and multiscale POD (mPOD). Unlike POD, mPOD is able to distinguish the most energetic modes at selected scales (or frequencies) by imposing spectral cutoffs to separate VLSM, large-scale motions (LSM), and small-scale motions. The VLSM can be clearly visualized from the most energetic spatial modes of the mPOD analysis at both Reynolds numbers. The mPOD results identify a new energetic mode that is aligned in the streamwise direction with a characteristic length covering the whole domain length. This new mode (called eVLSM mode) contains substantial energy, making it an important component of the VLSM in the flow field. The other energetic modes typically appear in pairs with specific streamwise phase shifts. The large-scale structures (apart from eVLSM) are inclined to the streamwise direction and appear to be responsible for the typical meandering behavior or even for the breakup of VLSM.

DOI: [10.1103/PhysRevFluids.7.084603](https://doi.org/10.1103/PhysRevFluids.7.084603)

## I. INTRODUCTION

Very-large-scale motions (VLSM) are a class of organized structures that have been identified relatively recently in a variety of wall-bounded turbulent flows [1–9]. VLSM are found in the logarithmic and wake regions of wall turbulence, and they are characterized by very long (of the order of  $10\delta$ ), meandering low- and high-speed regions. Here,  $\delta$  is the thickness of the boundary layer, the radius of the pipe or the channel half-height. These structures significantly impact near-wall flow properties and turbulent energy distributions, and their influence becomes more pronounced at higher Reynolds number [10–12]. VLSM can contain up to 60% of the cumulative fraction of the Reynolds shear stress [3,4,13] and they can have a large influence on turbulence statistics [14,15]. Here, we describe a new method to identify and describe VLSM, and to help analyze their features more precisely.

---

\*cheng.chi@ovgu.de

To explain the presence of VLSM, two main hypotheses have been proposed. In the first hypothesis, the VLSM are generated by the pseudo-streamwise alignment of large-scale motions (LSM) [1,3,9,16,17], and the instantaneous visualization of multiple LSM leading to the formation of a VLSM was demonstrated by Hutchins *et al.* [5], Lee *et al.* [9], and Dennis *et al.* [18]. In addition, VLSM are associated with the superposition and modulation of near-wall structures at smaller scale [5,7,19–22].

In the second hypothesis, the formation of VLSM are related to linear or nonlinear processes [13,23,24], while Flores *et al.* [25,26] claimed through numerical experiments that the out-layer dynamics are independent of the near-wall small-scale structures.

To examine these hypotheses, we need to distinguish VLSM from smaller-scale motions. This can be done by inspecting the premultiplied energy spectrum [1], where VLSM are seen to increase the energy content at long-wavelengths [8,10] and contribute to the formation of an outer peak in the spectrum [8,27,28]. Such an outer peak was also observed in the streamwise normal stress profile in the experiments by Morrison *et al.* [29], Hultmark *et al.* [12], and Samie *et al.* [30].

Alternatively, proper orthogonal decomposition (POD) analysis can be used to capture the most energetic contributions to the turbulent kinetic energy and to form a low-dimensional representation of the turbulent flow [13]. POD was first used to analyze turbulent flows by Lumley *et al.* [31], focusing on spatial modes. Later, snapshot POD was introduced by Sirovich *et al.* [32–34] to help accelerate the convergence of the spatial and temporal modes. Since then, POD has been widely used to analyze both experimental and numerical data. For example, Liu *et al.* [35] found that large-scale coherent motions in a turbulent channel flow can be reconstructed using only a few low-order POD modes. Wu *et al.* [36,37] further showed that for a turbulent boundary layer these low-order POD modes essentially capture the large-scale signature of the hairpin packets. POD was also used by Hellstrom *et al.* [13] to analyze turbulent pipe flows. They found that the 10 most energetic modes encompassed all the principal characteristics of the VLSM, and in later work they used POD to characterize the kinematics and dynamics of the LSM and VLSM in turbulent pipe flows [17,38–41], concluding that the VLSM were composed of trains of aligned LSM.

While POD ensures that the most energetic contributions are captured in the lower order modes, these modes still contain contributions from all frequencies (i.e., all scales). To refine the analysis, multiscale POD (mPOD) was proposed by Mendez *et al.* [42,43]. mPOD combines multiresolution analysis (MRA) and standard POD to obtain the energetic POD modes within a certain range of frequencies, and it was originally designed for flows that demonstrate clear scale separations. Here, we use mPOD for the first time (to the best of the authors understanding) to examine the structure of turbulent channel flows, thereby allowing a more precise visualization and analysis of VLSM, as marked by the identification of a new mode which is important for the understanding of VLSM. As noted by Mendez *et al.* [42], instead of filtering the correlation matrix, as in the spectral POD (sPOD) of Sieber *et al.* [44], mPOD decomposes it into the contributions of different scales using the multiresolution architecture (MRA) from wavelet theory. Also, instead of computing various eigenbases from the spectra of different portions of the data, as in the sPOD of Towne *et al.* [45], mPOD computes eigenbases on the correlation matrix of different scales. For the problem in the present study, we aim to separate different scales, such as VLSM, LSM and small-scale motions, considering the temporal modes and user-defined thresholds. This can be done with mPOD in a straightforward manner. By comparison, in the sPOD of Ref. [44] only a low-pass filter is used along the diagonals of the correlation matrix; a more complex scale separation can not be achieved in a straightforward manner. In the sPOD of Ref. [45], each mode is described by a single frequency, similar to DMD, while our objective is to separate between different frequency ranges (i.e., different temporal scales). Hence we have chosen mPOD for our study.

The numerical database is described in Sec. II, the analysis and discussion of the results are given in Sec. III, and the conclusions are presented in Sec. IV. Throughout the paper, the superscript  $+$  refers (as usual) to quantities normalized by the friction velocity  $u_\tau$  and the viscous wall unit  $l^* = \nu/u_\tau$ , where  $\nu$  is the kinematic viscosity. A summary of the notation used in this paper is given in Table I.

TABLE I. Notation.

| Notations                 | Descriptions                              |
|---------------------------|---|
| $f_n^+$                   | Normalized frequency coordinate           |
| $f_s (f_s^+)$             | Sampling frequency (normalized)           |
| $F_V (F_V^+)$             | Splitting frequency (normalized)          |
| $h$                       | half-width of channel                     |
| $k_x$                     | Streamwise wave number                    |
| $K (\hat{K})$             | Correlation matrix (Fourier transform of) |
| $l^*$                     | Viscous length scale                      |
| $P_k^+$                   | Production of kinetic energy              |
| $Re_b$                    | Bulk Reynolds number                      |
| $Re_\tau$                 | Friction Reynolds number                  |
| $t_F$                     | Flow-through time                         |
| $t_k$                     | Instantaneous time of the samples         |
| $u/v/w$                   | $x/y/z$ velocity fluctuations             |
| $U^+$                     | Mean streamwise velocity (normalized)     |
| $\overline{u^{2+}}$       | Streamwise turbulent intensity            |
| $U_b$                     | Bulk velocity                             |
| $u_\tau$                  | Friction velocity                         |
| $x/y/z$                   | Streamwise/wall-normal/spanwise direction |
| $y^+$                     | Normalized wall distance                  |
| $\phi$                    | Spatial mode                              |
| $\Phi_{uu}$               | Streamwise spectrum                       |
| $\eta$                    | Kolmogorov length scale near the wall     |
| $\lambda_x (\lambda_x^+)$ | Streamwise wavelength (normalized)        |
| $\nu$                     | Kinematic viscosity                       |
| $\psi (\hat{\psi})$       | Temporal mode (Fourier transform of)      |

## II. NUMERICAL DATABASE

Direct numerical simulations (DNS) were performed for fully developed turbulent flows in long channels using the incompressible version of the in-house hybrid finite-difference/spectral DNS solver DINO [46–48]. The code employs a sixth-order centered explicit scheme for spatial derivatives and a third-order explicit Runge-Kutta scheme for temporal integration. The Poisson equation for pressure is solved with spectral accuracy.

We consider two cases, Case A with  $Re_\tau = 906$  and Case B with  $Re_\tau = 3216$ , as summarized in Table II. Here,  $Re_\tau = hu_\tau/\nu$ , where  $h$  is the half-width of the channel and  $\nu = 1.557 \times 10^{-5}$

TABLE II. Summary of the two DNS cases. Here,  $U_b$  is the bulk velocity,  $Re_b = 2hU_b/\nu$  is the bulk Reynolds number,  $u_\tau$  is the friction velocity,  $Re_\tau$  is the friction Reynolds number,  $l^* = \nu/u_\tau$  is the viscous length scale, and  $\eta$  is the Kolmogorov length scale near the wall.

| Case | $Re_\tau$ | $Re_b$  | $U_b$ (m/s) | $u_\tau$ (m/s) | $l^*$ ( $\mu\text{m}$ ) | $\eta$ ( $\mu\text{m}$ ) |
|------|-----------|---------|-------------|----------------|-------------------------|--------------------------|
| A    | 906       | 38,432  | 23.9        | 1.12           | 13.8                    | 27.6                     |
| B    | 3216      | 153,330 | 23.9        | 1.00           | 15.5                    | 31                       |

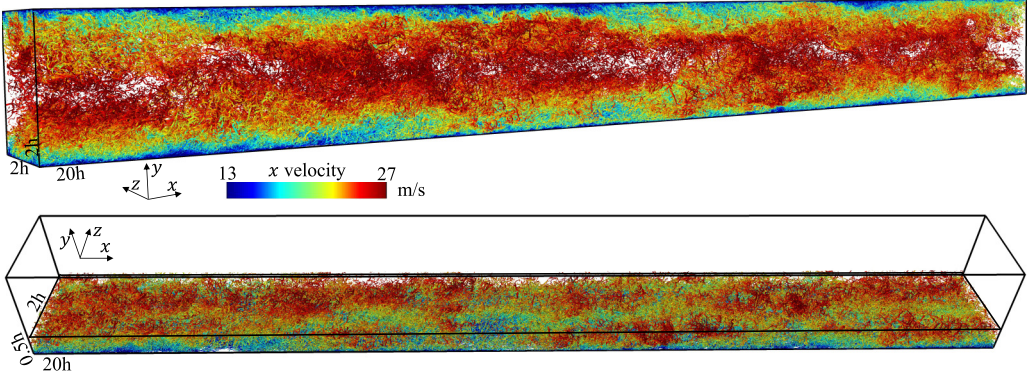


FIG. 1. Isosurface of  $Q$ -criterion with  $Q = 5 \times 10^6 \text{ s}^{-2}$  for a channel flow at  $\text{Re}_\tau = 3216$  (Case B) at  $t = 3.47t_F$  (where  $t_F = 20h/U_b$  is the flow-through time), colored by streamwise ( $x$ ) velocity.

$\text{m}^2/\text{s}$ . We use  $u$ ,  $v$ , and  $w$  to denote streamwise, wall-normal, and spanwise velocity fluctuations, respectively, corresponding to the  $x$ ,  $y$ , and  $z$  directions. No-slip conditions are applied to all channel walls. Case A has a domain of  $20h \times 2h \times 4h$  with  $h = 0.0125 \text{ m}$ . This domain is discretized by a grid measuring  $1024 \times 1025 \times 256$ , which is uniform in the streamwise and spanwise directions and stretched in the wall-normal direction. The final spatial resolution is  $\Delta x^+ = 17.56$ ,  $\Delta z^+ = 14.05$ , and  $0.35 \leq \Delta y^+ \leq 8.40$ . Case B has a domain measuring  $20h \times 2h \times 2h$  with  $h = 0.05 \text{ m}$ . This domain is discretized by a grid of  $4096 \times 2049 \times 512$ , with a final spatial resolution of  $\Delta x^+ = 15.68$ ,  $\Delta z^+ = 12.54$ , and  $0.54 \leq \Delta y^+ \leq 11.22$ . The resolutions of both cases are considered sufficient to capture the small scales, and the domains are long enough ( $20h$ ) to correctly capture VLSM and LSM.

Figure 1 shows a single realization of the full channel flow for Case B coloured by streamwise velocity on an isosurface of  $Q$ -criterion. The simulations were performed on the supercomputer JUWELS at the Juelich supercomputing center (JSC) using 8192 processors. In total, 8.4 million CPU hours were necessary for these two simulations, producing 3.4 TB of raw data for Case A and 45 TB of raw data for Case B. These data will be published and freely shared through the database of DFG Priority-Programme 1881 [49], so that other research groups are able to access it for further investigations on turbulence.

To give an overview of the large-scale structures in our test cases, Fig. 2 shows the isosurfaces of streamwise velocity fluctuations  $u$  (scaled by the friction velocity  $u_\tau$ ) at a wall distance  $y/h = 0.19$  for Case A and Case B. To achieve a fair comparison with Case B, only  $2h$  spanwise wide domain (from the full  $4h$  wide domain) has been chosen for all the analysis in Case A. The VLSM are evident

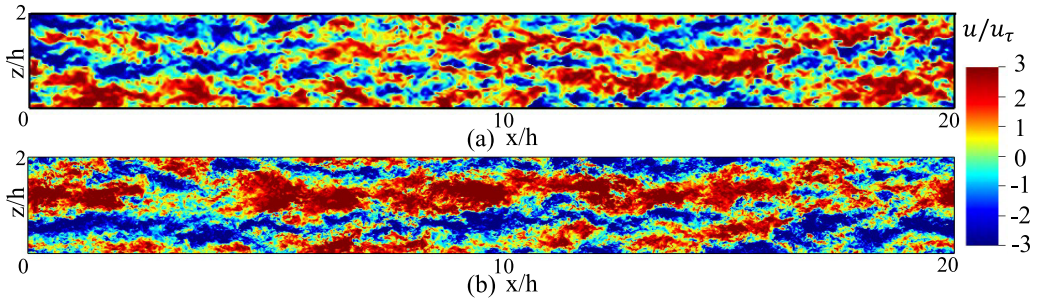


FIG. 2. Isosurfaces of velocity at  $y/h = 0.19$  for (a)  $\text{Re}_\tau = 906$  (Case A); (b)  $\text{Re}_\tau = 3216$  (Case B). For reference,  $U^+ \approx 18.5$  for Case A, and  $\approx 20$  for Case B.



in Case B by the low speed regions separated by high speed regions with streamwise lengths of the order of  $10h$ . These low and high speed regions can be also seen in Case A, with a similar spanwise spacing but possibly a shorter streamwise length than in Case B. The maximum velocity difference between low and high-speed regions is typically greater than  $\pm 15\%$ .

### III. ANALYSIS AND DISCUSSION

In the following sections, the overline  $\bar{q}$  means the average of the quantities over the  $x$ - $z$  plane, and the capital letter  $U$  indicates the temporally and spatially (over the  $x$ - $z$  plane) averaged statistics.

#### A. Turbulence statistics

The mean streamwise velocity  $U^+ = U/u_\tau$  profiles for the two cases are compared with previous studies in Fig. 3(a). The velocity profiles match well the results of Ref. [50], given that they were obtained at somewhat different values of the Reynolds number. Figure 3(b) shows the streamwise turbulence intensity  $\overline{u^{2+}}$  at different wall distances. The results follow the general trend with Reynolds number shown by previous data in the peak streamwise turbulence intensity and its position with increasing Reynolds number.

The premultiplied turbulent kinetic energy production is shown in Fig. 4 for five different Reynolds numbers. The area below each curve quantifies the contribution to turbulence production. At the lower Reynolds number, the major contribution to the production comes from the near-wall region (with a peak at  $y^+ \approx 20$ ), while the contribution from the logarithmic region increases with Reynolds number, demonstrating the increasingly important role of the LSM and VLSM.

#### B. Premultiplied spectrum analysis

To analyze the contributions of the larger scales to the total turbulence intensity, the premultiplied velocity spectra  $k_x \Phi_{uu}/u_\tau^2$  are shown in Fig. 5. Here,  $k_x$  is the streamwise wave number and  $\Phi_{uu}$  is the streamwise spectrum. For both Reynolds numbers the energy peak is found at nearly the same point ( $y^+ = 15$ ,  $\lambda_x^+ = 1000$ ), with  $\lambda_x^+$  the normalized streamwise wavelength. This peak is located at a wall distance where the maximum occurs in the turbulence intensity, and close to the peak in the premultiplied streamwise turbulence production, as demonstrated in Figs. 3 and 4.

At the higher Reynolds number, shown in Fig. 5(b), a second energy peak appears to emerge in the outer region, although it is also present, somewhat less prominently, at the lower Reynolds number. To gauge the energy distributions more precisely, Fig. 6 shows the contributions to the premultiplied spectrum sorted by wavelength. For Case A the second energy peak is located at  $\lambda_x^+ \approx 6000$ , while for Case B it is located at  $\lambda_x^+ \approx 12\,000$ . We see that the distributions near the wall are dominated by the small wavelength contributions, while this contribution becomes less and less important as  $y^+$  increases. This trend becomes more conspicuous at the higher Reynolds number [Fig. 6(b)]. For example in Case A at  $y^+ = 277$  ( $y/h = 0.19$ ), the contributions from large and small wavelength portions are comparable, whereas for Case B at  $y^+ = 602$  ( $y/h = 0.19$ ) the contributions from the large wavelengths begin to dominate.

As indicated by Önder and Meyers [51], the first and second peaks in Fig. 6 correspond to LSM and VLSM, respectively, when  $y^+ > 100$ . A spectral cutoff needs to be defined to make this demarcation, and a number of levels have been proposed in the literature. For example, Mathis *et al.* [19] used the cutoff  $\lambda_x/\delta = 1$  in the near-wall layer of the turbulent boundary layer, while Guala *et al.* [3] used  $\lambda_x/\delta = \pi$  in the outer layer of pipe flow where Bailey *et al.* [7] instead used  $\lambda_x/\delta = 2\pi$ . Based on the slope of the spectrum curve, the cutoff  $\lambda_x/\delta = 5$  was proposed by Önder and Meyers [51] in a turbulent boundary layer, whereas for turbulent channel flow Balakumar *et al.* [4] used  $\lambda_x/\delta = \pi$ . From Fig. 6 we see that for the current channel flow data the slopes of the premultiplied spectra begin to flatten at about  $\lambda_x/h = 1.65$  (corresponding to  $\lambda_x^+ = 1495$  for Case A and  $\lambda_x^+ = 5306$  for case B). Therefore, a cutoff at  $\lambda_x/h = 1.65$  was adopted in the present study to distinguish contributions due to LSM from those due to VLSM. Also a cutoff at  $\lambda_x/h = 0.88$

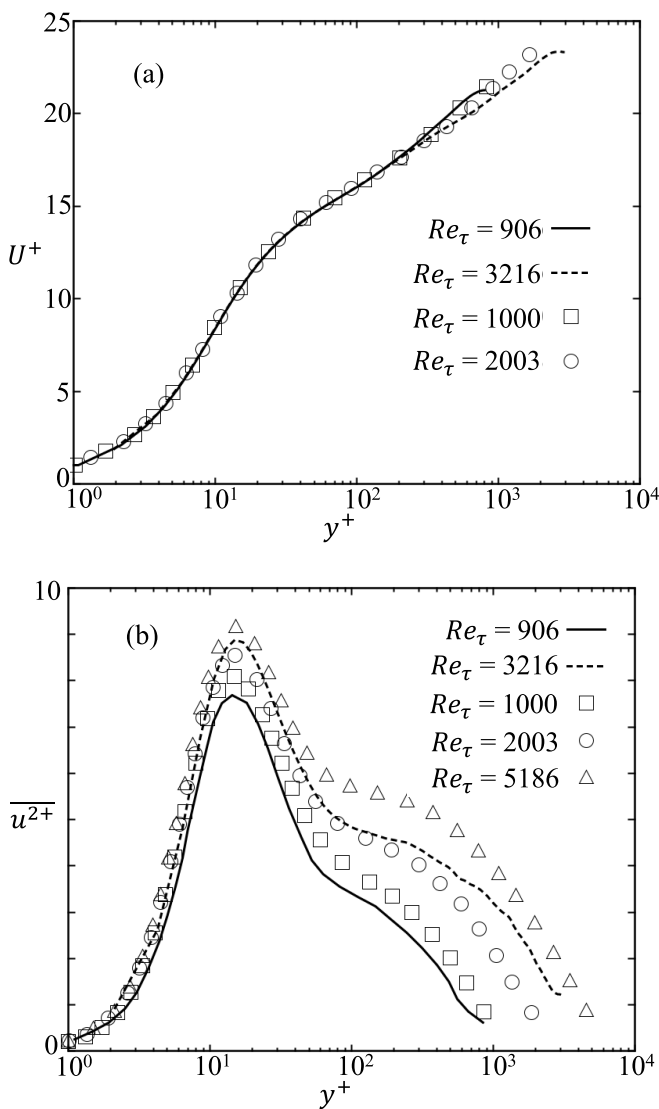


FIG. 3. Mean streamwise velocity (a) and streamwise turbulence intensity (b) at different wall-normal positions. The results for  $Re_\tau = 906$  (Case A) and  $3216$  (Case B), shown with continuous and dashed lines, respectively, are from the present DNS. The results for  $Re_\tau = 1000$ ,  $2003$ , and  $5186$  are taken from Ref. [50].

was adopted to distinguish contributions due to LSM from those due to small-scale motions (see Table III). The choice of these two cutoffs are confirmed in the later discussions.

### C. POD and mPOD analysis

To distinguish more clearly the LSM and VLISM, POD and mPOD were performed on 2D slices of the 3D DNS datasets  $\bar{\mathbf{u}}(\mathbf{x}, t_k) = [\mathbf{u}(\mathbf{x}, t_k), \mathbf{v}(\mathbf{x}, t_k), \mathbf{w}(\mathbf{x}, t_k)]$ . Here,  $\mathbf{x}$  indicates all the grid points in the 2D slices, and  $t_k$  indicates different time instants. The analysis is performed in a plane which is parallel to the wall, resulting in a uniform grid for  $\mathbf{x}$  (the grid is only stretched in wall-normal direction). The distribution of  $t_k$  is also uniform along the temporal axis, with  $t_{k+1} - t_k = \Delta t$ , where  $\Delta t = 1/f_s$  is the constant time step and  $f_s$  is the sampling frequency.

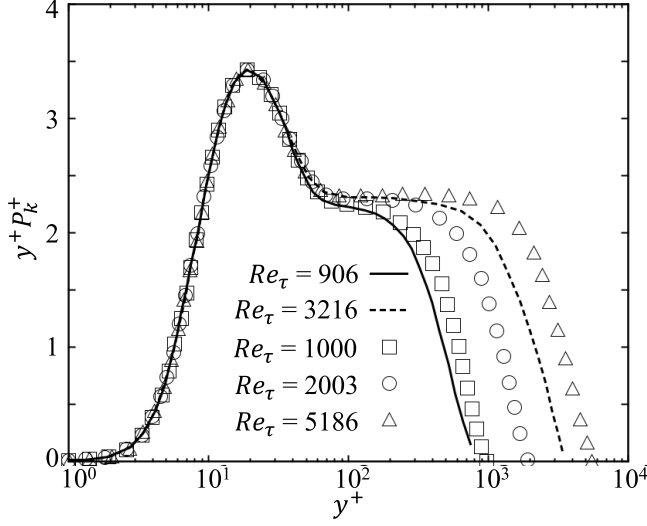


FIG. 4. Premultiplied turbulent kinetic energy production for different Reynolds numbers. Here  $P_k^+ = -\overline{uv}^+ dU^+/dy^+$  is the production of kinetic energy. The results for  $Re_\tau = 906$  (Case A) and 3216 (Case B), shown with continuous and dashed lines, respectively, are from the present DNS. The results for  $Re_\tau = 1000, 2003,$  and  $5186$  are taken from Ref. [50].

In POD the full spatial-temporal data  $\bar{\mathbf{u}}(\mathbf{x}, t_k)$  is decomposed into a linear combination of spatial structures  $\vec{\phi}_n(\mathbf{x})$  and temporal structures  $\psi_n(t_k)$ , where  $n$  is the mode number, so that

$$\bar{\mathbf{u}}(\mathbf{x}, t_k) = \sum_{n=1}^N \delta_n \vec{\phi}_n(\mathbf{x}) \psi_n(t_k), \quad (1)$$

where  $\delta_n$  is the corresponding mode amplitude. The rank  $N = \min(n_s, n_t)$  is the full rank, with  $n_s = n_p \times n_u$ , where  $n_p$  is the number of grid points,  $n_u$  is the number of velocity components, and  $n_t$  is the number of snapshots. In this manner,  $\bar{\mathbf{u}}(\mathbf{x}, t_k)$  can be transformed into a  $n_s \times n_t$  matrix  $D$ , with columns containing the data in space and rows containing the data in time. A compact form of Eq. (1) is thus obtained as

$$D = \phi \delta \psi^T, \quad (2)$$

where  $\delta = \text{diag}[\delta_1, \delta_2, \dots, \delta_N]$  is the diagonal matrix containing the energy contribution of each mode, the superscript  $T$  denotes matrix transposition, and  $\phi = [\phi_{x1}, \dots, \phi_{xN}, \phi_{y1}, \dots, \phi_{yN}, \phi_{z1}, \dots, \phi_{zN}]$ , where the subscripts  $x, y$  and  $z$  denote the three velocity component directions. Finally,  $\psi = [\psi_1, \dots, \psi_N]$ .

POD sorts on the energy contribution of each mode, which is done by taking the temporal structures  $\psi$  as eigenvectors of the correlation matrix  $K = D^\dagger D$ , where the superscript  $\dagger$  indicates a conjugate transpose. In this way,

$$K = \psi \lambda \psi^T. \quad (3)$$

Here, the correlation matrix  $K$  is symmetric and positive definite. The temporal structures are orthonormal. If  $D$  is real, as considered in this work, Eq. (2) yields

$$K = D^\dagger D = \psi \delta \phi^T \phi \delta \psi^T. \quad (4)$$

Thus,

$$\lambda = \delta \phi^T \phi \delta. \quad (5)$$

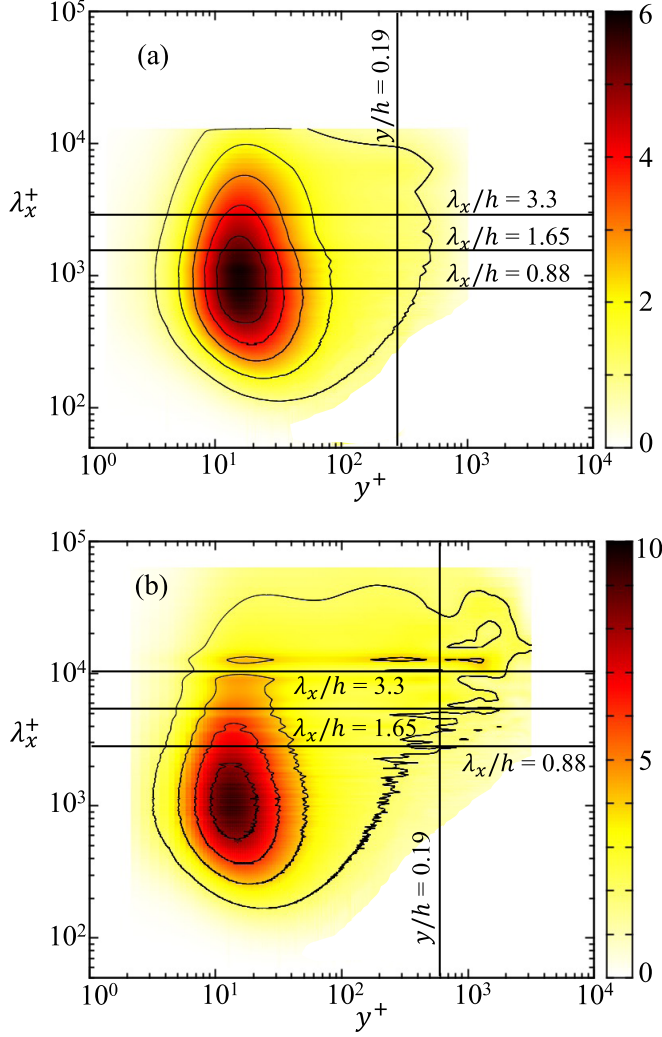


FIG. 5. Premultiplied spectra of streamwise velocity fluctuations as a function of  $y^+$  and  $\lambda_x^+$ . (a) Case A,  $\text{Re}_\tau = 906$ ; (b) Case B,  $\text{Re}_\tau = 3216$ .

Since  $\lambda$  is diagonal,  $\phi^T \phi = I$  and  $\lambda = \delta^2$ . As a consequence, the spatial structures are also real and orthonormal; they correspond to the eigenvectors of the correlation matrix  $C = DD^T$ . The energy contribution of each mode becomes the square-root of the eigenvalues of the correlation matrix.

In contrast to POD, the temporal structures of mPOD are computed by adding spectral constraints to the classical POD. To this end, the correlation matrix  $K$  is grouped into contributions from different scales by multiresolution analysis (MRA), as also done in wavelet analysis [52]. A transfer function  $H_m$  (a vector with size  $n_t$ ) is proposed to select a given scale  $m$  (frequencies ranging from  $f_{m1}$  to  $f_{m2}$ ).  $H_m$  is set to 1 for the frequencies within scale  $m$ , and 0 otherwise. For ideal conditions, the transfer functions satisfy  $\sum_{m=1}^M H_m = 1$  and  $H_i \odot H_j = 0 \ \forall i \neq j$ , where  $M$  is the total number of scales and  $\odot$  denotes the entry-by-entry product. Because a sharp frequency cutoff is difficult to implement at lower frequencies, smoothing transfer functions were used following the approach described in Ref. [42]. The remaining spectral overlap between the transfer function of adjacent scales appears to be small enough to allow a clear scale separation. To use the transfer function

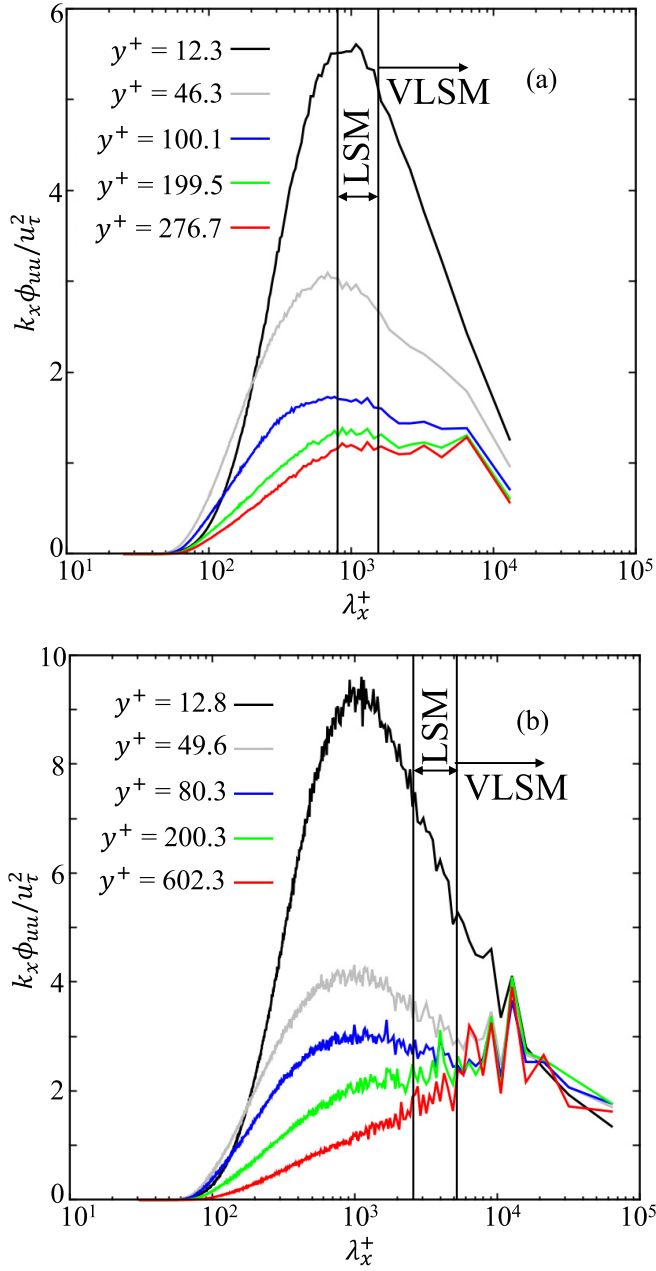


FIG. 6. Premultiplied spectra of streamwise velocity fluctuations as a function of  $\lambda_x^+$ . (a) Case A,  $Re_\tau = 906$  ( $y^+ = 276.7$  corresponds to  $y/h = 0.19$ ); (b) Case B,  $Re_\tau = 3216$  ( $y^+ = 602.3$  corresponds to  $y/h = 0.19$ ). The vertical lines are at  $\lambda_x/h = 0.88$  and  $1.65$ .

properly, it needs to be copied row-wise to create a matrix  $H'_m$  with size  $n_s \times n_t$ . The splitting of the correlation matrix is then achieved as

$$K = \sum_{m=1}^M K^{(m)} = \sum_{m=1}^M \Psi_F [\hat{K} \odot H'_m] \Psi_F, \quad (6)$$



TABLE III. Splitting frequencies for Cases A and B.

| Case | $Re_\tau$ | $F_V^+ \times 10^3$ | $F_V h/U_b$ | $\lambda_x^+$ | $\lambda_x/h$ |
|------|-----------|---------------------|-------------|---------------|---------------|
| A    | 906       | 6.23                | 0.264       | 2970          | 3.3           |
|      |           | 12.46               | 0.528       | 1485          | 1.65          |
|      |           | 23.36               | 0.986       | 792           | 0.88          |
| B    | 3216      | 1.88                | 0.252       | 10613         | 3.3           |
|      |           | 7.07                | 0.948       | 2830          | 0.88          |

where  $\hat{K} = \overline{\Psi}_F K \overline{\Psi}_F$  is the 2D Fourier transform of  $K$ ,  $\Psi_F[i, j] = \exp(2\pi q/n_t)^{(i-1) \times (j-1)}$  is the Fourier matrix, with  $q^2 = -1$  and  $i, j \in [1, n_t]$ . The overbar denotes complex conjugation, and  $H'_m = H_m'^T H'_m$  is the 2D transfer function. After splitting, POD can be done for each scale separately as

$$K^{(m)} = \psi^{(m)} \lambda^{(m)} \psi^{(m)T}. \quad (7)$$

Then, all the eigenvalues are sorted in decreasing order and the eigenvectors are re-arranged into a single matrix. The correlation matrices at each scale are kept symmetric, and so the eigenvectors are orthonormal. A perfect spectral splitting ensures orthogonality of the final temporal matrix. More detailed information concerning mPOD is given by Mendez *et al.* [42].

#### D. Results for Case A

For the lower Reynolds number Case A ( $Re_\tau = 906$ ), 254 snapshots were used for the analysis with a sampling frequency  $f_s^+ = f_s \nu / u_\tau^2 = 0.1559$  and  $f_s h / U_b = 6.569$ . The 2D slice at wall distance  $y/h = 0.19$  was selected since it is located in the outer region, nominally near the end of the logarithmic region, although at these Reynolds numbers the logarithmic region is not yet fully formed [53,54]. Here, the sampling wavelength is  $\lambda_x^+ = U^+ / f_s^+ = 118.78$ . At this wall distance, as shown in Fig. 6(a), the spectral contributions from different scales are comparable. For mPOD, three splitting frequencies were chosen as  $F_V^+ = [6.23, 12.46, 23.36] \times 10^{-3}$ , which correspond to  $F_V h / U_b = [0.264, 0.528, 0.986]$ ,  $\lambda_x^+ = [2970, 1485, 792]$ , and  $\lambda_x/h = [3.3, 1.65, 0.88]$ ; see Table III. These values were chosen based on the cutoffs defined in Sec. III B and the Fourier transform of the full temporal mode shown in Fig. 7, where the dominant frequencies can be identified. The cutoffs at  $\lambda_x/h = 0.88$  and 1.65 separate VLSM from LSM, and LSM from small-scale motions,

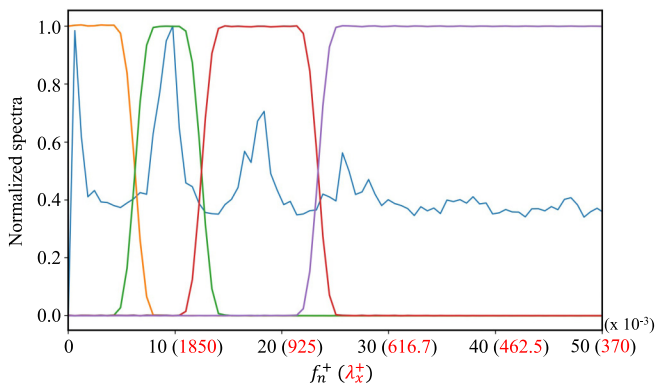


FIG. 7. Fourier transform of the complete temporal information (diagonal of  $\hat{K}$ ) for Case A at  $y/h = 0.19$ , and corresponding transfer functions for the four selected frequency ranges (colored lines) corresponding to  $F_V^+ \times 10^3 = 6.23, 12.46, \text{ and } 23.36$ . See Table III.

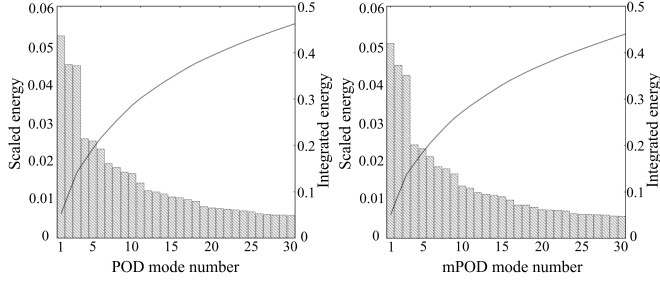


FIG. 8. Scaled energy for Case A at  $y/h = 0.19$  of the first 30 most energetic POD modes (left) and mPOD modes (right). The integrated energy with increasing mode number is shown by the solid line.

but a third cutoff at  $\lambda_x/h = 3.3$  is also used based on the results in Fig. 7 that suggest the presence of structures even longer than VLSM.

Figure 8 shows the scaled energy content of the 30 most energetic POD and mPOD modes. The distribution among modes is similar for POD and mPOD, with substantial energy (15% of the total energy) contained in the first three modes. The temporal modes for POD and mPOD, however, display significant differences. First, Fig. 9 shows the Fourier transform of the temporal modes, demonstrating that mPOD clearly separates the temporal structures in different frequency ranges for its 1st and 2nd mode, while the 1st and 2nd POD modes are mixed and overlap with each other in frequency space. Second, Fig. 10 shows the temporal modes themselves. The primary difference between mPOD and POD is in the 1st temporal mode. Here, mPOD removes the smaller scales (with typical  $\lambda_x^+ \approx 1850$ ,  $\lambda_x/h \approx 2$ ) and retains only the larger scales, while the 1st temporal POD mode is mixed and involves both large and small scales. The 2nd mPOD mode also shows more regularity than the 2nd POD mode.

The spatial modes of POD and mPOD are given in Fig. 11. For both mPOD and POD, some modes come in pairs, as in the 2nd and 3rd modes, the 4th and 5th modes, and the 7th and 8th modes. The pairs have a similar energy content (see Fig. 8), and a streamwise phase shift that is about half the length of a typical structure, so that each member of a given pair overlaps the other to some extent. The spatial arrangement of the pairs is consistent with the evolutionary cycle of large-scale motion described by Hellström *et al.* [17], or possibly the presence of helical modes. Note that the spatial structures in the 2nd modes of mPOD and POD [Figs. 11(c) and 11(k)] have the opposite sign, which is due to the opposite sign of the temporal structure in the 2nd POD and mPOD modes as shown in Figs. 10(b) and 10(d).

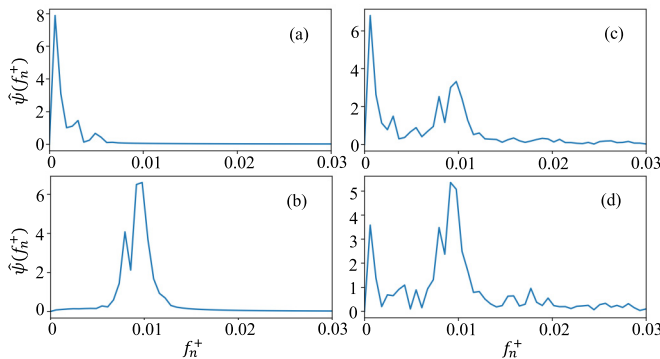


FIG. 9. Fourier transform of temporal modes for Case A at  $y/h = 0.19$ : (a) mPOD 1st mode; (b) mPOD 2nd mode; (c) POD 1st mode; (d) POD 2nd mode.

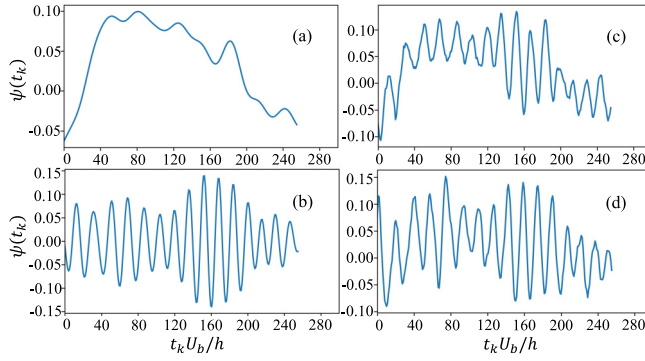


FIG. 10. Temporal modes for Case A at  $y/h = 0.19$ : (a) mPOD 1st mode; (b) mPOD 2nd mode; (c) POD 1st mode; (d) POD 2nd mode.

The primary differences between the mPOD and POD modes are in the 1st and 6th modes, which do not have a corresponding pair. Long and straight coherent structures appear in the 1st mPOD mode with a length that covers the full domain, much longer than that typically associated with VLSM. A similar behavior is seen in the 6th mode, albeit with a reduced spanwise spacing. The corresponding POD modes, however, indicate meandering structures with lengths that are closer to  $10h$ . The temporal filtering inherent in mPOD therefore suggests that these streamwise invariant

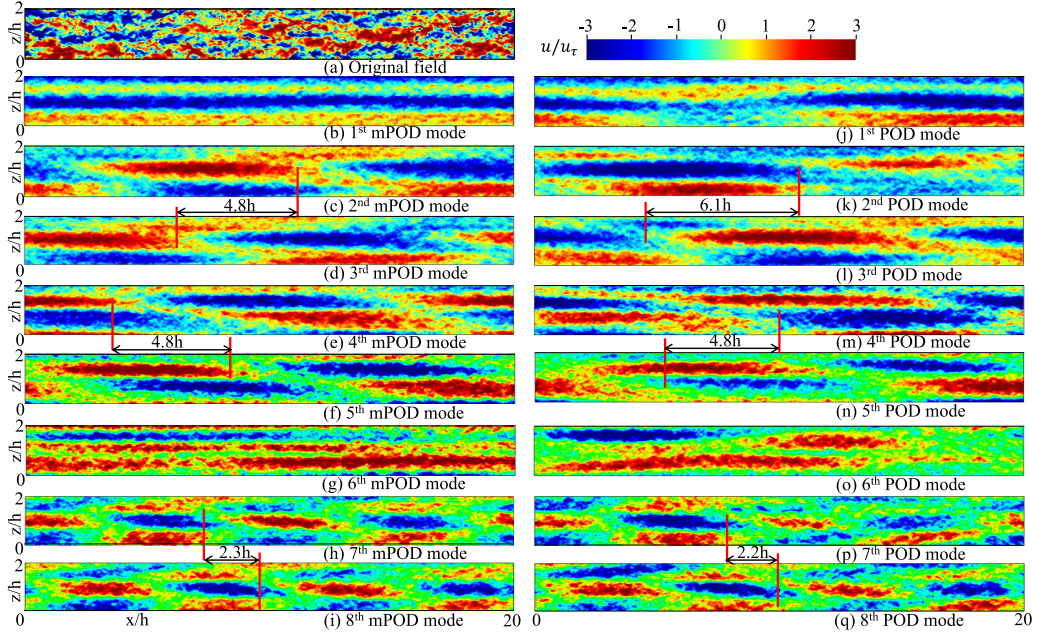


FIG. 11. Spatial modes for Case A at  $y/h = 0.19$ . (a) Original streamwise velocity fluctuation flow field; (b) 1st mPOD mode; (c) 2nd mPOD mode; (d) 3rd mPOD mode; (e) 4th mPOD mode; (f) 5th mPOD mode; (g) 6th mPOD mode; (h) 7th mPOD mode; (i) 8th mPOD mode; (j) 1st POD mode; (k) 2nd POD mode; (l) 3rd POD mode; (m) 4th POD mode; (n) 5th POD mode; (o) 6th POD mode; (p) 7th POD mode and (q) 8th POD mode. Note that the 1st and 6th mPOD modes have  $\lambda_x/h \geq 3.3$ ; the 2nd, 3rd, 4th, and 5th mPOD modes have  $1.65 \leq \lambda_x/h < 3.3$ ; the 7th and 8th mPOD modes have  $0.88 \leq \lambda_x/h < 1.65$ .

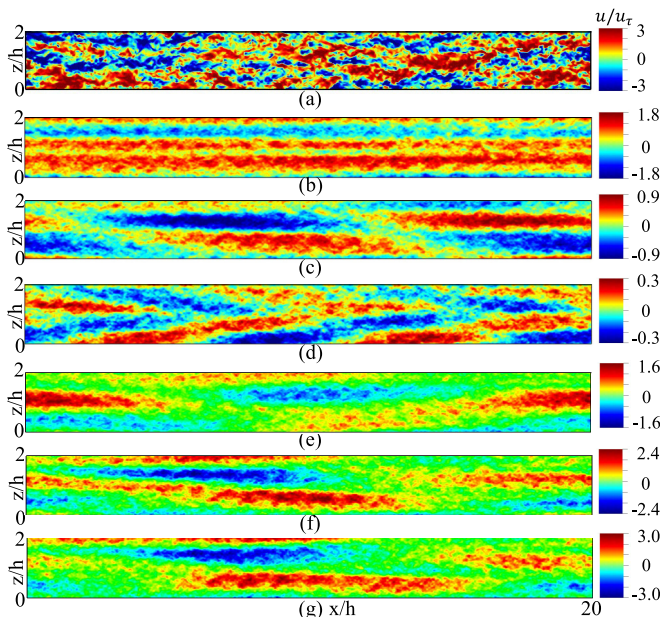


FIG. 12. Reconstructed streamwise velocity fluctuation flow field for Case A at  $y/h = 0.19$ . (a) Original velocity field; (b) reconstructed field using the 4 most energetic mPOD modes with  $f_n^+ \leq 6.23 \times 10^{-3}$  ( $\lambda_x/h \geq 3.3$ ); (c) using the 4 most energetic mPOD modes with  $6.23 \times 10^{-3} < f_n^+ \leq 12.46 \times 10^{-3}$  ( $1.65 \leq \lambda_x/h < 3.3$ ); (d) using the 4 most energetic mPOD modes with  $12.46 \times 10^{-3} < f_n^+ \leq 23.36 \times 10^{-3}$  ( $0.88 \leq \lambda_x/h < 1.65$ ); (e) using the 4 most energetic POD modes; (f) using the 8 most energetic POD modes; (g) using the 12 most energetic POD modes.

spatial modes, not previously identified in channel flows, are an important part of the most energetic motions. In what follows, we will call these streamwise invariant spatial modes “extended VLISM” (eVLISM).

It is important to note that we have labeled the coherent structures in the decomposed modes as VLISM, LSM, and small-scale motions using their typical streamwise lengths. These structures, however, are component contributions to the full velocity field. For example, the VLISM and LSM seen in the full velocity field are the sum of the decomposed modes. Therefore, identification of the new mode eVLISM does not necessarily identify a new coherent structure in the original flow field.

As to the characteristic lengths of the other modes, the 7th and 8th mPOD modes have lengths in the range  $2-4h$ , which are typical for LSM, while for the 2nd, 3rd, 4th and 5th mPOD mode they are  $8-10h$ , which are in the range expected for VLISM. This result confirms that the cutoff at  $\lambda_x/h = 1.65$  is a good choice for distinguishing between VLISM and LSM. By combining the results shown in Figs. 9 and 11, it can be inferred that the 1st POD mode represents a combination of VLISM (with typical streamwise length of  $8-10h$ ) and eVLISM, resulting in meandering structures with shorter length than the full channel length. This is particularly evident for the lowest high speed streak in Fig. 11(k).

In the pipe flow results given by Ref. [13], the LSM with typical length  $4h$  were observed in the 2nd POD mode, while such coherent structures appear first in the 7th POD mode in the channel flow considered here. One reason might be the relatively short temporal window (equivalent to about  $20R$  in length) in Ref. [13] make the 1st mode over-represented. Another reason could be the lower Reynolds number for the pipe flow, where  $Re_\tau = 354$  compared to 906 for the channel flow Case A.

The reconstructed flow field using the most energetic modes within different scales are shown in Fig. 12. eVLISM (typical length covering the domain length  $20h$ ) can be clearly identified from the

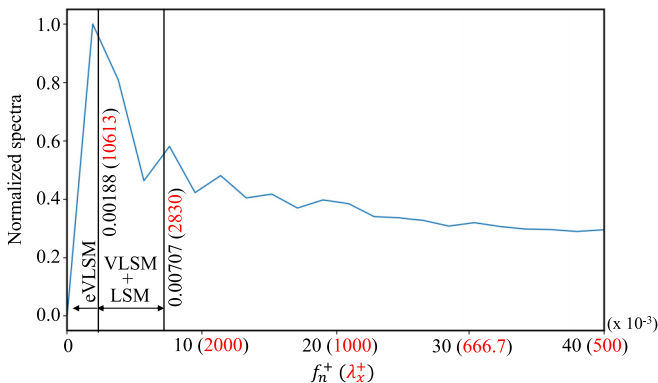


FIG. 13. Fourier transform of the complete temporal information for Case B at  $y/h = 0.19$ .

reconstruction using the four most energetic mPOD modes with  $f_n^+ \leq 6.23 \times 10^{-3}$  ( $\lambda_x/h \geq 3.3$ ). VLSM with a typical length of  $8\text{--}10h$  appear in the reconstruction using the four most energetic mPOD mode with  $6.23 \times 10^{-3} < f_n^+ \leq 12.46 \times 10^{-3}$  ( $1.65 \leq \lambda_x/h < 3.3$ ). LSM with typical length of  $2\text{--}4h$  can be identified from the reconstruction using the four most energetic mPOD mode with  $12.46 \times 10^{-3} < f_n^+ \leq 23.36 \times 10^{-3}$  ( $0.88 \leq \lambda_x/h < 1.65$ ). Hence, with the help of mPOD the coherent structures at different scales are clearly separated. Furthermore, it can be observed that the reconstructed structures in Fig. 12(c) are slightly inclined to the streamwise direction, with an angle of approximately  $5^\circ$ , which may be related to the helix angle of  $5^\circ$  seen for the most energetic POD mode in pipe flow [41]. The structures in Fig. 12(d) are inclined with an angle of approximately  $10^\circ$ . The meandering of the VLSM observed in the original flow field is clearly identified with the spanwise tilt of the LSM, as seen in Fig. 12(d). In contrast, with POD the reconstructions using the 4, 8, and 12 most energetic modes are much less informative regarding the role of these different scales [see Figs. 12(e)–12(g)].

### E. Results for Case B

For the higher Reynolds number Case B ( $\text{Re}_\tau = 3216$ ), 103 snapshots were used with  $f_s^+ = f_s v/u_\tau^2 = 0.0489$  and  $f_s h/U_b = 6.56$ . As in Case A, the 2D slice at a wall distance  $y/h = 0.19$  is considered in the analysis. Here, the sampling wavelength is  $\lambda_x^+ = U^+/f_s^+ = 409$ . In mPOD, the splitting frequency is set to  $F_V^+ = [1.88, 7.07] \times 10^{-3}$ , which corresponds to the scale separation wavelength at  $\lambda_x^+ = [10613, 2830]$  and  $\lambda_x/h = [3.3, 0.88]$ , as shown in Table III. Due to the limited number of snapshots for this case, the cutoff at  $\lambda_x/h = 1.65$  used in Case A could not be applied,

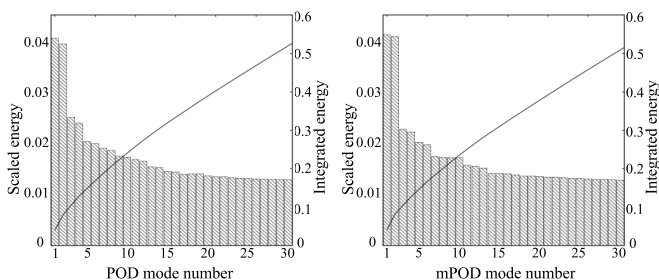


FIG. 14. Scaled energy for Case B at  $y/h = 0.19$  of the first 30 most energetic POD modes (left) and mPOD modes (right). The integrated energy with increasing mode number is shown by the solid line.



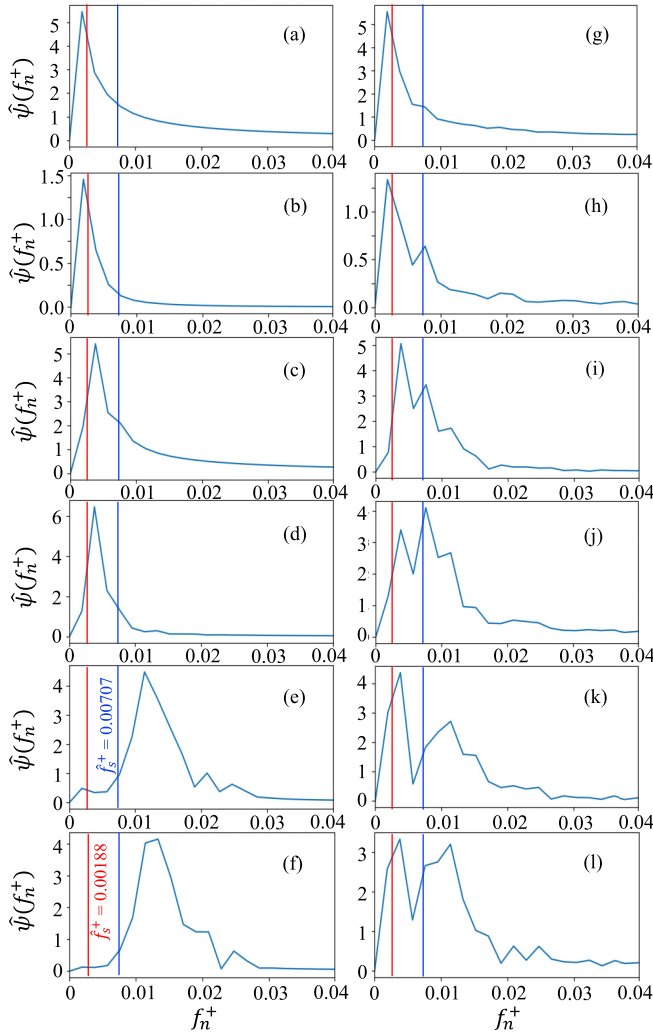


FIG. 15. Fourier transform of temporal modes for Case B at  $y/h = 0.19$ : (a–f) mPOD 1st to 6th mode; (g–l) POD 1st to 6th mode. For  $f_n^+ = 0.00188$ ,  $\lambda_x/h = 3.3$  and for  $f_n^+ = 0.00707$ ,  $\lambda_x/h = 0.88$ .

so that our analysis for Case B is restricted to examining the eVLSM and the combined mode of VLSM and LSM.

Figure 13 shows the Fourier transform of the complete temporal information. The normalized spectrum broadly decreases as  $\lambda_x^+$  decreases although some small, localized peaks occur. In contrast to Case A (Fig. 7), the spectrum does not exhibit obvious spectral peaks that could help identify the various large scale motions.

Figure 14 shows the scaled energy content of the 30 most energetic POD and mPOD modes for Case B. The distributions for mPOD and POD modes are very similar, and some modal pairs can be observed with comparable energy content.

The first 6 temporal modes for mPOD and POD are given in Figure 15. The scale separation in mPOD is much cleaner than in POD, and in mPOD we see a distinct classification for modes 1 and 2 ( $f_n^+ \leq 0.00188$ ,  $\lambda_x/h \geq 3.3$ ), modes 3 and 4 ( $0.00707 \geq f_n^+ > 0.00188$ ,  $0.88 \leq \lambda_x/h < 3.3$ ), and modes 5 and 6 ( $f_n^+ > 0.00707$ ,  $\lambda_x/h < 0.88$ ). In contrast, the POD modes are more mixed.

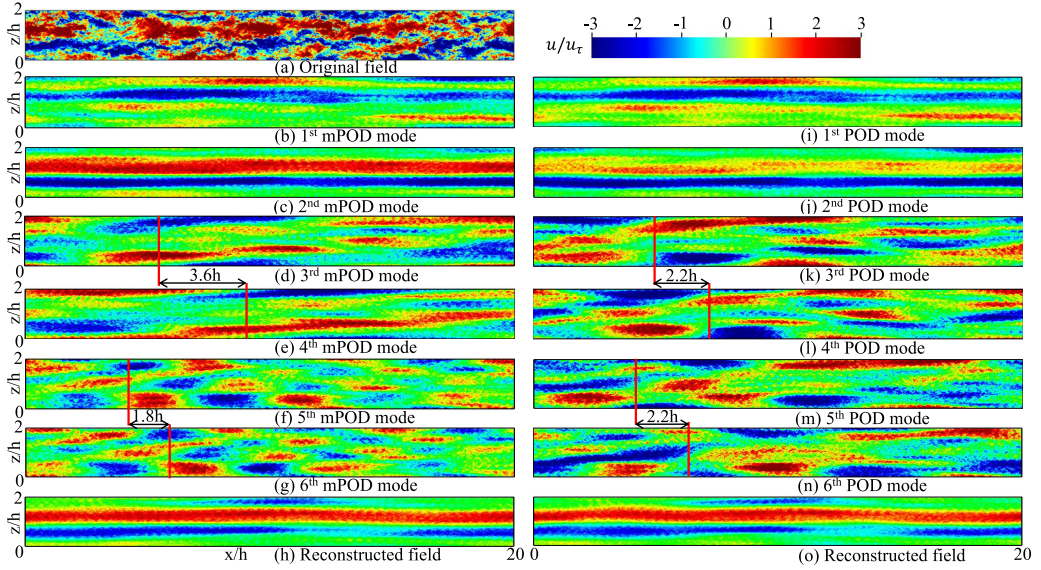


FIG. 16. Spatial modes for Case B at  $y/h = 0.19$ . (a) Original streamwise velocity fluctuation flow field; (b) spatial structures of the 1st mPOD mode; (c) the 2nd mPOD mode; (d) the 3rd mPOD mode; (e) the 4th mPOD mode; (f) the 5th mPOD mode; (g) the 6th mPOD mode (h) reconstructed streamwise velocity fluctuation flow field using the first four mPOD modes; (i) the 1st POD mode; (j) the 2nd POD mode; (k) the 3rd POD mode; (l) the 4th POD mode; (m) the 5th POD mode; (n) the 6th POD mode; (o) reconstructed streamwise velocity fluctuation flow field using the first four POD modes. Note that the 1st and 2nd mPOD modes have  $\lambda_x/h \geq 3.3$ ; the 3rd and 4th mPOD modes have  $0.88 \leq \lambda_x/h < 3.3$ , and the 5th and 6th mPOD modes have  $\lambda_x/h < 0.88$ .

The first six spatial modes for both mPOD and POD are shown in Fig. 16, together with the reconstructed velocity fields using the first four modes. The 1st and 2nd modes make a pair, and show relatively straight and very long coherent structures (covering the domain length). Similar structures were seen in Case A and dubbed eVLSM. although in that case the first mode did not have a pair (this is discussed further below). The 1st mPOD and POD modes are broadly similar, but the 2nd mPOD mode is much more defined than the 2nd POD mode. The 3rd and 4th mPOD modes make up another pair, with a streamwise shift of about  $3.6h$ , a typical length of  $8\text{--}12h$  (indicative of VLSM), and a slight inclination to the streamwise direction. The 3rd and 4th POD modes also form a pair, in this case with a streamwise shift of about  $2.2h$ , but they appear to be more of a mix of shorter ( $\sim 3h$ ) and longer structures ( $\sim 6\text{--}8h$ ). The next pair is made up of the 5th and 6th modes, where the mPOD modes show distinct structures with a typical length less than  $2h$  (indicative of small-scale motions) and a streamwise shift of about  $1.8h$ . The 5th and 6th POD modes, as for the 3rd and 4th POD modes, seem to be a mix of shorter ( $\sim 3h$ ) and longer structures ( $\sim 6\text{--}8h$ ), although they have a consistent streamwise shift of approximately  $2.2h$ .

As noted earlier, in Case A the eVLSM mode is the 1st mPOD mode while in Case B it is a pair made up of the 1st and 2nd mPOD modes. Although it is not clear why this is so, one possibility is that this eVLSM mode evolves with Reynolds number. For example, the combined energy content of the 1st and 2nd mPOD modes in Case B is approximately 0.08 of the total energy, whereas the 1st mPOD mode in Case A contains only 0.05 of the total energy. Another possibility is the limited spanwise width of the domain, where periodic boundary conditions are enforced. In Case A, that width is  $4h$  (only  $2h$  is shown in Fig. 11) but in Case B it is only  $2h$ . Comparing Figs. 11(b) and 16(b), 16(c) it is likely that the smaller domain width imposes constraints on the spanwise length scales which could lead to changes in the inferred modes.

The inclined structures in the 3rd and 4th mPOD modes have a typical angle of  $5^\circ$  to the streamwise direction. This is consistent with Fig. 12(c) in Case A for VLSM. Comparing the original flow field (especially for the low-speed streaks) with the inclined structures in the 3rd and 4th mPOD modes, similar tilt angles are observed, and this inclination of the modes could be the main reason for meandering features of the VLSM. The reconstruction using the first four mPOD modes combines eVLSM and the inclined VLSM. As is seen from Fig. 16(h), the inclined VLSM terminate the very long structure in the streamwise direction (see the low-speed streak) and the reconstructed field is dominated by eVLSM, which contain much more energy than the smaller scale motions. The reconstructed fields using the first four modes are very similar for mPOD and POD, primarily because the 1st and 2nd modes contain considerably more energy than the 3rd and 4th modes (as also seen from Fig. 14), and these two most energetic modes are similar for POD and mPOD.

#### IV. CONCLUSIONS

DNS for turbulent channel flows at  $Re_\tau = 906$  and  $3216$  was used to compare mPOD and POD for the visualization and analysis of VLSM. The premultiplied spectra analysis showed that a second kinetic energy peak exists at a higher wave number in the outer region at both Reynolds numbers, suggesting a possible mixing of different scales when using energy-based decomposition such as POD. Multiscale POD (mPOD) was found to help separate different scales and to provide a more detailed analysis of the individual contribution from different scales. In particular, a new energetic mode (eVLSM) was identified by mPOD, which is aligned in the streamwise direction with a characteristic length covering the full  $20h$  domain length. This eVLSM mode was found to be the most energetic mode at both Reynolds numbers, and therefore crucial for the VLSM representation in the full flow field. Mode pairs were seen to be more distinct in mPOD modes, with each member of the pair displaying very similar temporal and spatial mode shapes and specific streamwise phase shifts. The streamwise phase shift in each mode pair make the reconstructed structures (as shown in Case A) or combined mode structures (as shown in Case B) inclined to the streamwise direction that are consistent with the meandering features of VLSM in the original flow field. Furthermore, the inclined structures are able to terminate the VLSM, as shown in Case B.

#### ACKNOWLEDGMENTS

This work is supported by the Priority Programme SPP 1881 Turbulent Superstructures of the Deutsche Forschungsgemeinschaft (DFG). The DNS simulations were made possible thanks to the Gauss Centre for Supercomputing e.V. [55], providing computing time on the Supercomputer JUWELS (under project “dnschannelfsp”) at Jülich Supercomputing Centre (JSC, Germany). A.J.S. acknowledges support under ONR Grants No. N00014-17-1-2309 and No. N00014-19-1-2301.

- 
- [1] K. C. Kim and R. J. Adrian, Very large-scale motion in the outer layer, *Phys. Fluids* **11**, 417 (1999).
  - [2] C. D. Tomkins and R. J. Adrian, Energetic spanwise modes in the logarithmic layer of a turbulent boundary layer, *J. Fluid Mech.* **545**, 141 (2005).
  - [3] M. Guala, S. E. Hommema, and R. J. Adrian, Large-scale and very-large-scale motions in turbulent pipe flow, *J. Fluid Mech.* **554**, 521 (2006).
  - [4] B. J. Balakumar and R. J. Adrian, Large- and very-large-scale motions in channel and boundary-layer flows, *Philos. Trans. R. Soc. A* **365**, 665 (2007).
  - [5] N. Hutchins and I. Marusic, Evidence of very long meandering features in the logarithmic region of turbulent boundary layers, *J. Fluid Mech.* **579**, 1 (2007).
  - [6] J. P. Monty, J. Stewart, R. Williams, and M. S. Chong, Large-scale features in turbulent pipe and channel flows, *J. Fluid Mech.* **589**, 147 (2007).

- [7] S. C. C. Bailey and A. J. Smits, Experimental investigation of the structure of large- and very-large-scale motions in turbulent pipe flow, *J. Fluid Mech.* **651**, 339 (2010).
- [8] J. P. Monty, N. Hutchins, H. C. H. NG, I. Marusic, and M. S. Chong, A comparison of turbulent pipe, channel and boundary layer flows, *J. Fluid Mech.* **632**, 431 (2009).
- [9] J. H. Lee and H. J. Sung, Very-large-scale motions in a turbulent boundary layer, *J. Fluid Mech.* **673**, 80 (2011).
- [10] I. Marusic, R. Mathis, and N. Hutchins, High Reynolds number effects in wall turbulence, *Int. J. Heat Fluid Flow* **31**, 418 (2010).
- [11] A. J. Smits, B. J. McKeon, and I. Marusic, High-Reynolds number wall turbulence, *Annu. Rev. Fluid Mech.* **43**, 353 (2011).
- [12] M. Hultmark, M. Vallikivi, S. C. C. Bailey, and A. J. Smits, Turbulent Pipe Flow at Extreme Reynolds Numbers, *Phys. Rev. Lett.* **108**, 094501 (2012).
- [13] L. H. O. Hellström, A. Sinha, and A. J. Smits, Visualizing the very-large-scale motions in turbulent pipe flow, *Phys. Fluids* **23**, 011703 (2011).
- [14] B. Ganapathisubramani, E. K. Longmire, and I. Marusic, Characteristics of vortex packets in turbulent boundary layers, *J. Fluid Mech.* **478**, 35 (2003).
- [15] A. J. Smits, M. Hultmark, M. Lee, S. Pirozzoli, and X. Wu, Reynolds stress scaling in the near-wall region of wall-bounded flows, *J. Fluid Mech.* **926**, A31 (2021).
- [16] J. Lee, J. H. Lee, J.-I. Choi, and H. J. Sung, Spatial organization of large- and very-large-scale motions in a turbulent channel flow, *J. Fluid Mech.* **749**, 818 (2014).
- [17] L. H. O. Hellström, B. Ganapathisubramani, and A. J. Smits, The evolution of large-scale motions in turbulent pipe flow, *J. Fluid Mech.* **779**, 701 (2015).
- [18] D. J. C. Dennis and T. B. Nickels, Experimental measurement of large-scale three-dimensional structures in a turbulent boundary layer. Part 2. Long structures, *J. Fluid Mech.* **673**, 218 (2011).
- [19] R. Mathis, N. Hutchins, and I. Marusic, Large-scale amplitude modulation of the small-scale structures in turbulent boundary layers, *J. Fluid Mech.* **628**, 311 (2009).
- [20] R. Mathis, J. P. Monty, N. Hutchins, and I. Marusic, Comparison of large-scale amplitude modulation in turbulent boundary layers, pipes, and channel flows, *Phys. Fluids* **21**, 111703 (2009).
- [21] B. Ganapathisubramani, N. Hutchins, J. P. Monty, D. Chung, and I. Marusic, Amplitude and frequency modulation in wall turbulence, *J. Fluid Mech.* **712**, 61 (2012).
- [22] S. Duvvuri and B. J. McKeon, Triadic scale interactions in a turbulent boundary layer, *J. Fluid Mech.* **767**, R4 (2015).
- [23] J. C. del Álamo and J. Jimenez, Linear energy amplification in turbulent channels, *J. Fluid Mech.* **559**, 205 (2006).
- [24] B. J. McKeon and A. S. Sharma, A critical-layer framework for turbulent pipe flow, *J. Fluid Mech.* **658**, 336 (2010).
- [25] O. Flores and J. Jimenez, Effect of wall-boundary disturbances on turbulent channel flows, *J. Fluid Mech.* **566**, 357 (2006).
- [26] O. Flores, J. Jimenez, and J. C. Del Álamo, Vorticity organization in the outer layer of turbulent channels with disturbed walls, *J. Fluid Mech.* **591**, 145 (2007).
- [27] S. Hoyas and J. Jiménez, Scaling of the velocity fluctuations in turbulent channels up to  $Re_\tau = 2003$ , *Phys. Fluids* **18**, 011702 (2006).
- [28] P. Schlatter and R. Örlü, Assessment of direct numerical simulation data of turbulent boundary layers, *J. Fluid Mech.* **659**, 116 (2010).
- [29] J. F. Morrison, B. J. McKeon, W. Jiang, and A. J. Smits, Scaling of the streamwise velocity component in turbulent pipe flow, *J. Fluid Mech.* **508**, 99 (2004).
- [30] M. Samie, I. Marusic, N. Hutchins, M. K. Fu, Y. Fan, M. Hultmark, and A. J. Smits, Fully resolved measurements of turbulent boundary layer flows up to  $Re_\tau = 20,000$ , *J. Fluid Mech.* **851**, 391 (2018).
- [31] J. L. Lumley, *Atmospheric Turbulence and Radio Wave Propagation*, edited by A. M. Yaglom and V. I. Tatarski (1967), pp. 166–178.
- [32] L. Sirovich, Turbulence and the dynamics of coherent structures: I. Coherent structures; II. Symmetries and transformations; III. Dynamics and scaling, *Q. Appl. Math.* **45**, 561 (1987).

- [33] L. Sirovich, Chaotic dynamics of coherent structures, *Physica D* **37**, 126 (1989).
- [34] L. Sirovich, Analysis of turbulent flows by means of the empirical eigenfunctions, *Fluid Dyn. Res.* **8**, 85 (1991).
- [35] Z. Liu, R. J. Adrian, and T. J. Hanratty, Large-scale modes of turbulent channel flow: Transport and structure, *J. Fluid Mech.* **448**, 53 (2001).
- [36] Y. Wu and K. T. Christensen, Spatial structure of a turbulent boundary layer with irregular surface roughness, *J. Fluid Mech.* **655**, 380 (2010).
- [37] Y. Wu, A study of energetic large-scale structures in turbulent boundary layer, *Phys. Fluids* **26**, 045113 (2014).
- [38] L. H. O. Hellström and A. J. Smits, The energetic motions in turbulent pipe flow, *Phys. Fluids* **26**, 125102 (2014).
- [39] L. H. O. Hellström, I. Marusic, and A. J. Smits, Self-similarity of the large-scale motions in turbulent pipe flow, *J. Fluid Mech.* **792**, R1 (2016).
- [40] L. H. Hellström and A. J. Smits, Structure identification in pipe flow using proper orthogonal decomposition, *Philos. Trans. R. Soc. A* **375**, 20160086 (2017).
- [41] J. R. Baltzer, R. J. Adrian, and X. Wu, Structural organization of large and very large scales in turbulent pipe flow simulation, *J. Fluid Mech.* **720**, 236 (2013).
- [42] M. A. Mendez, M. Balabane, and J.-M. Buchlin, Multi-scale proper orthogonal decomposition of complex fluid flows, *J. Fluid Mech.* **870**, 988 (2019).
- [43] M. A. Mendez, D. Hess, B. B. Watz, and J.-M. Buchlin, Multiscale proper orthogonal decomposition (mPOD) of TR-PIV data—A case study on stationary and transient cylinder wake flows, *Meas. Sci. Technol.* **31**, 094014 (2020).
- [44] M. Sieber, C. O. Paschereit, and K. Oberleithner, Spectral proper orthogonal decomposition, *J. Fluid Mech.* **792**, 798 (2016).
- [45] A. Towne, O. T. Schmidt, and T. Colonius, Spectral proper orthogonal decomposition and its relationship to dynamic mode decomposition and resolvent analysis, *J. Fluid Mech.* **847**, 821 (2018).
- [46] A. Abdelsamie, G. Fru, T. Oster, F. Dietzsch, G. Janiga, and D. Thévenin, Towards direct numerical simulations of low-Mach number turbulent reacting and two-phase flows using immersed boundaries, *Comput. Fluids* **131**, 123 (2016).
- [47] C. Chi, A. Abdelsamie, and D. Thévenin, A directional ghost-cell immersed boundary method for incompressible flows, *J. Comput. Phys.* **404**, 109122 (2020).
- [48] A. Abdelsamie, G. Lartigue, C. E. Frouzakis, and D. Thévenin, The Taylor–Green vortex as a benchmark for high-fidelity combustion simulations using low-Mach solvers, *Comput. Fluids* **223**, 104935 (2021).
- [49] J. Schumacher *et al.*, DFG—Priority Programme 1881: Turbulent Superstructures, <https://www.tu-ilmeneau.de/universitaet/fakultaeten/fakultaet-maschinenbau/profil/institute-und-fachgebiete/fachgebiet-stroemungsmechanik/dfg-priority-programme-1881-turbulent-superstructures> (2022).
- [50] M. Lee and R. D. Moser, Direct numerical simulation of turbulent channel flow up to  $Re_\tau \approx 5200$ , *J. Fluid Mech.* **774**, 395 (2015).
- [51] A. Önder and J. Meyers, On the interaction of very-large-scale motions in a neutral atmospheric boundary layer with a row of wind turbines, *J. Fluid Mech.* **841**, 1040 (2018).
- [52] S. G. Mallat, *A Wavelet Tour of Signal Processing* (Elsevier LTD, Oxford, 2009).
- [53] B. J. McKeon, J. Li, W. Jiang, J. F. Morrison, and A. J. Smits, Further observations on the mean velocity distribution in fully developed pipe flow, *J. Fluid Mech.* **501**, 135 (2004).
- [54] A. J. Smits, Batchelor Prize Lecture: Measurements in wall-bounded turbulence, *J. Fluid Mech.* **940**, A1 (2022).
- [55] See, [www.gauss-centre.eu](http://www.gauss-centre.eu).